Dissociative recombination without curve crossings: NeH^+ and ArH^+

Åsa Larson *
Department of Physics, Stockholm University, AlbaNova University Center, S-10691 Stockholm, Sweden

Ann E. Orel
Department of Chemical Engineering, University of California, Davis, California 95616, USA

(Received 21 November 2025; accepted 17 February 2026; published 5 March 2026)

Experiments on dissociative recombination on ArH^+ show a small but nonzero cross section at low collision energies. Therefore, dissociative recombination of ArH^+, as well as NeH^+, is studied theoretically. Accurate *ab initio* fixed-nuclei electron-scattering calculations are performed to produce *S*-matrices that are used as input into a multichannel quantum defect treatment of the dissociation process. Results are compared to available experimental data.

DOI: 10.1103/fvmr-4cs8

I. INTRODUCTION

Dissociative recombination (DR) involves the capture of an electron by a molecular ion into an excited resonant state that dissociates into neutral fragments. The process is more efficient when the potential of a resonant state crosses the ion ground state near its equilibrium geometry, leading to the so-called direct mechanism of dissociative recombination. The electron can be captured directly into the resonant state, the "direct process," or captured into a rovibrationally excited Rydberg state of the neutral molecule that couples to the dissociative resonant state, which eventually predissociates, the "indirect process." If the direct process is dominant, the indirect mechanism has a small effect on the cross section. However, in particular, at low energy the indirect process can dominate. Note that both these processes rely on a dissociative state, usually a member of a Rydberg series converging to an excited state of the ion, that is energetically available.

In the HeH system, such a resonant dissociative state does not exist. However, it was found that the low-energy DR rate is nonzero [1]. There have been extensive experimental and theoretical studies of this system [2–5]. It has been shown that recombination can occur at a significant rate for a system that lacks suitable curve crossings if there are strong nonadiabatic interactions between the Rydberg states and the ionization continuum of the ion ground state [2,3].

One of us previously studied DR of NeH^+ [6,7] and found that this system also does not have a curve crossing between the potentials of the ion ground state and a repulsive neutral state in the region where the vibrational ($v = 0$) wave function of the target ion is nonzero. At low energies, DR is not driven by the direct process. At higher energies, electronic resonant states are available, and the calculated cross section agreed well with experiment [6]. In the experiment, the absolute DR cross section was not measured. The resonances were found to be lower in energy than in the $HeH^+ + e^-$ system, which may be an indication that, as was found in dissociative recombination of rare gas dimer ions [8–10], the energy difference between the potentials of the doubly excited resonant states and the ion ground state will get smaller as the atomic number increases. The effect of the nonadiabatic couplings among the Rydberg states converging to the ground state of the ion was not considered for NeH^+ [7]. The Rydberg states of NeH have been studied *ab initio* using multireference configuration interaction (MRCI) calculations [11–13]. Quantum defects have been extracted [12,13], and nonadiabatic coupling elements among the Rydberg states have been computed [11,13].

On the experimental side, the DR cross section of ArH^+ ions, with electron energies from 0 to 30 eV, was measured at the Aarhus STorage Ring In Denmark (ASTRID) by Mitchell *et al.* [14]. They found that ArH^+ does have a significant recombination rate above 2.5 eV, displaying several peaks at higher energies. Theoretical studies of the system agreed well with experiment and showed no low-energy DR [15,16]. However, recent experiments using the Cryogenic Storage Ring (CSR) [17] performed with ArH^+ ions in the ground vibrational state and in cold rotational states found that there is a nonzero cross section at low energies [18]. The Rydberg states of ArH were previously studied *ab initio* (see [19] and references therein), and quantum defects were extracted.

In this paper we present our results for low-energy DR with ArH^+ and NeH^+ and compare them to available experiments. To describe electron capture to Rydberg states of the target ions and to compute the DR cross sections, we use the multichannel quantum defect theory (MQDT) following an approach similar to the one applied to DR of CH^+ by Forer *et al.* [20]. Calculations of the DR cross section require accurate fixed-nuclei *S*-matrices at low scattering energies. The electron-scattering calculations are performed with the

*Contact author: aasal@fysik.su.se

Published by the American Physical Society under the terms of the Creative Commons Attribution 4.0 International license. Further distribution of this work must maintain attribution to the author(s) and the published article's title, journal citation, and DOI. Funded by Bibsam.

complex Kohn variational method, implemented in the MESA code [21].

In the next section, we briefly discuss the method used to obtain fixed-nuclei S-matrices. From the S-matrix, quantum defects can be extracted. In Sec. III, we outline the MQDT method used to compute DR cross sections, and the results are reported in Sec. IV for the ArH^+, ArD^+, NeH^+, and NeD^+ ions. Calculated cross sections are compared to available experimental findings. Atomic units are used throughout the article.

II. FIXED-NUCLEI S-MATRIX

Electron-scattering calculations using the complex Kohn variational method [22,23] at fixed internuclear distances are performed to obtain the S-matrices needed for the MQDT calculations. Since this method has been described elsewhere (see [22,23] and references therein), we will only summarize it here. The method uses a stationary principle for the T-matrix:

$$T_{\text{stat}} = T_{\text{trial}} - 2\int \Psi(\hat{H} - E)\Psi, \tag{1}$$

with the trial wave function being

$$\Psi = \hat{A}[\Phi(\mathbf{r}_1, \ldots, \mathbf{r}_N)F(\mathbf{r}_{N+1})] + \sum_{\mu} d_\mu \Theta_\mu(\mathbf{r}_1, \ldots, \mathbf{r}_{N+1}). \tag{2}$$

Since we are here interested in low energy scattering, only one ($X^1\Sigma$) energetically open electronic N-electron target state is included as the wave function Φ. The operator $\hat{A}$ antisymmetrizes the coordinates of the incident electron with those of the target electrons. The second term with the sum (Q space) in Eq. (2) contains Θ_μ, which are square-integrable $(N+1)$-electron configuration-state functions (CSFs). The $(N+1)$-electron CSFs describe short-range correlation and the effects of closed channels and contain information about the resonance portion of the scattering wave function. Both penetration terms [22,23] needed to relax any constraints implied by the orthogonality of the scattered wave to the target orbitals and configuration-interaction relaxation terms [22,23] are used to construct the Q space.

In order to carry out the scattering calculations, an accurate target wave function using compact molecular orbitals is required. This is achieved by carrying out a larger MRCI calculation on the ground-state ion to obtain natural orbitals that are then used in a smaller MRCI calculation to obtain the target wave function.

For NeH^+, the neon basis set is the double zeta plus polarization of Dunning and Hay [24] with an extra set of diffuse functions: seven s functions with exponents of 0.1, 0.05, 0.025, 0.010, 0.005, 0.002, and 0.001, four p functions (0.07, 0.035, 0.015, 0.007), and two d functions (1.5, 0.5). For hydrogen the basis set of Siegbahn and Liu [25] is used, expanded with an extra set of diffuse functions: two s functions (0.022, 0.006), three p functions (0.05, 0.0125, 0.0035), four d functions (0.12, 0.036, 0.011, 0.003), and one f function (0.0023). The initial orbitals are obtained from a diagonalization of the core Hamiltonian. These orbitals are then used in an all singles and doubles configuration interaction (CI) calculation on the ion from an active space of five orbitals, the 1σ, 2σ, 3σ, and degenerate 1π orbitals, to obtain the natural orbitals. Eight natural orbitals with the largest occupation numbers are selected: 1σ–4σ and 1π–2π. The lowest orbital (1σ) is kept doubly occupied, and the final target wave function is obtained from a MRCI calculation with reference configurations generated by excitations of eight electrons among the other seven orbitals. For the $(N+1)$-electron system, an extra electron is added to the reference states generated from the MRCI calculations in the target space of the seven orbitals.

To obtain reliable S-matrices and quantum defects, the electron-scattering calculations should be performed with the origin at the center of charge of the target ion [26,27]. Setting the origin at the center of charge will, in general, result in a better unitarity of the fixed-nuclei S-matrix and quantum defects with weaker energy dependences [27]. To obtain this, a structure calculation is first carried out on the target ion in the center-of-mass frame, and the dipole moment is then calculated. It is used to determine the center of charge. Then the calculations are performed with the center of charge as the origin. This process is repeated for each geometry.

A similar procedure is used for ArH^+. The basis set for hydrogen is the same as that in the NeH^+ calculation. For argon, the basis set of McLean and Chandler [28] is used, augmented with an extra set of diffuse functions: seven s functions with exponents of 0.1, 0.05, 0.025, 0.01, 0.005, 0.002, and 0.001 and four p functions with exponents of 0.07, 0.035, 0.015, and 0.007. In this case, the 1σ, 2σ, 3σ, and 1π orbitals (composed primarily of $1s$, $2s$, and $2p$ argon atomic orbitals) are kept doubly occupied, and the reference space is composed of 4σ, 5σ, 2π, and 6σ. Single and double external excitations are included when calculating the natural orbitals. Twelve natural orbitals with the largest occupation numbers are selected: 1σ–6σ and 1π–3π. The 1σ, 2σ, 3σ, and 1π orbitals are kept doubly occupied, and the active space is composed of the remaining seven orbitals and eight electrons. In the MRCI, single external excitations are included. A similar procedure is used to obtain the center of charge like in the NeH^+ calculation.

In both cases, the MRCI wave function determined is used as the target wave function $\Phi(\mathbf{r}_1, \ldots, \mathbf{r}_N)$ in Eq. (2). By inserting the trial wave function into the complex Kohn functional [23], the unknown coefficients in the trial wave function can be optimized, including the T-matrix. From the T-matrix, the fixed-nuclei elastic scattering matrix $S^{\Lambda}_{lm,l'm'}(\epsilon, R)$ can be obtained. Angular momenta up to $l = 2$ and $|m| = 1$ are included in the calculations. The electron-scattering calculations are carried out in overall $^2A_1$, $^2A_2$, and $^2B_1$ symmetries in C_{2v} to obtain the S-matrices in the $^2\Sigma^+$, $^2\Pi$, and $^2\Delta$ symmetries in $C_{\infty v}$. The calculations are carried out using the MESA program [21].

III. MQDT

The goal is to compute the low-energy (<2.0 eV) DR cross sections. For both NeH^+ and ArH^+, the low-energy DR is driven by electron capture to rovibrationally excited Rydberg states [13,18], and the MQDT method is suitable for describing the process. We will follow the approach developed by Greene and coworkers [3,20,29]. The fixed-nuclei electron-scattering calculations are performed including only

the ground target wave function as described in Sec. II since the focus is the low-energy DR cross section and electron capture into electronic resonant states becomes important only at higher collision energies. The S-matrix elements $S^{\Lambda}_{lm,l'm'}(\epsilon, R)$ are computed in overall symmetries $\Lambda = {}^2\Sigma^+$, ${}^2\Pi$, and ${}^2\Delta$, for internuclear distances $R \in [1.0, 6.0]a_0$ for NeH^+ and $R \in [1.5, 5.0]a_0$ for ArH^+. These are the regions where the $v = 0$ vibrational wave functions of the target ions are nonzero. For each internuclear distance, the S-matrices are computed for scattering energies ranging from 0.001 to 0.01 H. The S-matrix elements are labeled with the (l, m) quantum numbers of the incoming and scattered electrons.

The MQDT approach here applied to compute the DR cross section requires the fixed-nuclei S-matrix to be perfectly unitary, $\mathbf{S}^\dagger\mathbf{S} = \mathbf{1}$. Using the complex Kohn variational method, the S-matrix is not unitary by construction. To obtain a unitary S-matrix, for each internuclear distance and scattering energy, the S-matrix is used to compute the K-matrix:

$$\mathbf{K} = i\frac{\mathbf{1}-\mathbf{S}}{\mathbf{1}+\mathbf{S}}. \tag{3}$$

If the S-matrix is unitary, the K-matrix is symmetric (and real). This is enforced using $\tilde{\mathbf{K}} = \frac{1}{2}(\mathbf{K} + \mathbf{K}^T)$. The K-matrix is then diagonalized, $\mathbf{U}^T\tilde{\mathbf{K}}\mathbf{U}$, and the eigenvalues of the K-matrix $\tan[\delta_\alpha(R, \epsilon)]$ are related to the "eigenquantum defects" $\mu^\alpha(R)$ according to

$$\lim_{\epsilon\to 0}\delta_\alpha(R,\epsilon) = \lim_{n\to\infty}\pi\mu^\alpha_n(R) = \pi\mu^\alpha(R). \tag{4}$$

The quantum defect matrix can be constructed using the similarity transformation of the diagonal matrix containing the eigenquantum defects, according to $\mu = \mathbf{U}\mu^\alpha\mathbf{U}^T$. Finally, a fixed-nuclei S-matrix that is exactly unitary can be constructed by the transformation $\tilde{\mathbf{S}} = \mathbf{U}\exp(i2\pi\mu^\alpha)\mathbf{U}^T$.

In the following, we use the S-matrices calculated at the lowest scattering energy, $\epsilon = 0.001$ H, for both the NeH^+ and ArH^+ ions to obtain the eigenquantum defects $\mu^\alpha(R)$ and to compute the unitary S-matrices. Thus, the energy dependences of the quantum defects are presently neglected.

In the MQDT method, the scattering matrix for inelastic scattering

$$XH^+(v, j) + e^- \to XH^+(v', j') + e^-$$

(with X = Ne or Ar) is obtained by a rovibrational frame transformation [30]. In the first step, the vibrational frame transformation is performed, in which the matrix elements

$$\begin{aligned} S^{\Lambda}_{v'l'm',\mathrm{vlm}} &= \left\langle \Phi^L_{v'} \middle| S^{\Lambda}_{l'm',lm} \middle| \Phi^R_v \right\rangle \\ &= \int \Phi^L_{v'}(R) S^{\Lambda}_{l'm',lm}(R) \Phi^R_v(R) dR \end{aligned} \tag{5}$$

are computed. To describe dissociation via Rydberg states, we do not employ box-normalized vibrational eigenstates of the target ion associated with the potential $V_{\mathrm{ion}}(R)$. Instead, we use bound and continuum eigenstates obtained with exterior complex scaling [31,32], in which the radial coordinate is rotated into the complex plane at large internuclear distances:

$$R \to \tilde{R} = \begin{cases} R & R < R_0, \\ R_0 + (R - R_0)e^{i\theta} & R > R_0. \end{cases} \tag{6}$$

Here, R_0 is the distance where the potential has reached its asymptotic value. In the present calculations, $R_0 = 10.0a_0$ and $\theta = 30^\circ$ are used, and the vibrational eigenstates are calculated by using a finite-element method employing a discrete-variable representation [32,33]. Since the Hamiltonian $\hat{H} = -\frac{1}{2\mu}\frac{d^2}{d\tilde{R}^2} + V_{\mathrm{ion}}(\tilde{R})$ is not Hermitian, the energy eigenvalues for states above the dissociation limit will be complex,

$$\tilde{E}_v = \left\langle \Phi^L_v \middle| \hat{H} \middle| \Phi^R_v \right\rangle = E_v - i\gamma_v, \tag{7}$$

and the corresponding wave functions will decay at distances $R > R_0$. Note the labeling with superscripts L/R on the vibrational eigenstates since the biorthogonal eigenstates [34] are used for the non-Hermitian Hamiltonian. For both NeH and ArH, 50 vibrational eigenstates are used in the frame transformation.

An alternative description of dissociation through Rydberg states can be obtained using a complex absorbing potential (CAP) [20]. In this approach, an imaginary term is added to the potential at large internuclear distances when the vibrational eigenstates of the target ion are calculated. We tested this method employing CAP potentials and parameters from [35] and found that the resulting dissociative recombination cross sections are in very good agreement with those obtained using exterior complex scaling.

In the next step, the rotational part of the frame transformation is performed using the Clebsch-Gordan coefficients [30] to compute the full S-matrix in the laboratory frame as [20,36]

$$\begin{aligned} &S^J_{v'j'\mu'l',vj\mu l} \\ &\quad = \sum_{\Lambda}\sum_{m,m'}(-1)^{l+m+l'+m'} C^{j'\mu'}_{l'-m',J\Lambda} S^{\Lambda}_{v'l'm',\mathrm{vlm}} C^{j\mu}_{l-m,J\Lambda}. \end{aligned} \tag{8}$$

Here, J is the quantum number of the total angular momentum for the reaction complex, j is the quantum number of the total angular momentum of the target ion, and l is the electron angular momentum, with $\hat{\mathbf{J}} = \hat{\mathbf{j}} + \hat{\mathbf{l}}$. Λ, μ, and m are the quantum numbers for the projections onto the molecular axis with $\hat{J}_z = \hat{j}_z + \hat{l}_z$. Here, we consider NeH^+ and ArH^+ $X^1\Sigma^+$ target states, and hence, $\mu = 0$. The full S-matrix is block diagonal in J. For the NeH system, 20 rotational states of the target ion are considered, while for ArH, 10 rotational states are included.

In the MQDT framework, closed channels are eliminated, and the physical S-matrix is computed. For a given total energy E, the full S-matrix is separated into blocks of open and closed channels,

$$\mathbf{S}^J = \begin{pmatrix} \mathbf{S}_{\mathrm{oo}} & \mathbf{S}_{\mathrm{oc}} \\ \mathbf{S}_{\mathrm{co}} & \mathbf{S}_{\mathrm{cc}} \end{pmatrix}. \tag{9}$$

The physical S-matrix is then computed using [20]

$$\mathbf{S}^{J,\mathrm{phys}}(E) = \mathbf{S}_{\mathrm{oo}} - \mathbf{S}_{\mathrm{oc}}(\mathbf{S}_{\mathrm{cc}} - e^{-2i\beta})^{-1}\mathbf{S}_{\mathrm{co}}. \tag{10}$$

Here, the diagonal matrix β has the elements

$$\beta_{ij}(E) = \frac{\pi}{\sqrt{2(E_i - E)}}\delta_{ij}, \tag{11}$$

where E_i is the rovibrational energy of closed channel i, calculated as

$$E_i = \tilde{E}_{v_i} + B_v J(J+1) - D_v J^2(J+1)^2. \tag{12}$$

Experimental rotational constants for NeH^+ [37] and ArH^+ [38–40] and their isotopologues are used.

The Hermitian adjoint of the physical S-matrix $\mathbf{S}^{J,\mathrm{phys}\dagger}(E)$ is computed as described in [20]. Since exterior complex scaling is used when the vibrational eigenstates are computed, the elements of the β-matrix in (11) are complex, and the physical S-matrix is not unitary. The DR cross section [for a target ion in rovibrational state (v_0, j_0)] is given by [20]

$$\sigma_{v_0 j_0 \mu_0}(E) = \sum_J \frac{\pi}{2E}\frac{(2J+1)}{(2j_0+1)} \times \sum_l \left[1 - \sum_{v' j' \mu' l'} S^{J,\mathrm{phys}}_{v' j' \mu' l', v_0 j_0 \mu_0 l} S^{J,\mathrm{phys}\dagger}_{v_0 j_0 \mu_0 l, v' j' \mu' l'}\right]. \tag{13}$$

In the ion–storage-ring experiments, the molecular ions are in the lowest vibrational state ($v_0 = 0$). For the comparison with measurements, the populations of the rotational states are considered by calculating the average DR cross section $\tilde{\sigma} = \sum_{j_0} p_{j_0} \sigma_{v_0 j_0 \mu_0}$, where p_{j_0} is the population of rotational state j_0 of the target ion. In the CSR experiment on ArH^+, the rotational states $j_0 = 0$, 1, and 2 are populated [41]. To make a comparison with the measured DR rate,

$$\alpha^{mb} = \langle \tilde{\sigma} v \rangle \tag{14}$$

is calculated, where v is the electron-ion collision velocity and the angle brackets designate the average over the velocity distribution in the electron-ion overlap region [41].

IV. RESULTS

A. NeH^+

To analyze the fixed-nuclei scattering matrix, the adiabatic quantum defects are extracted from the eigenvalues of the S-matrix according to

$$\mu^\alpha(R) = \frac{\delta_\alpha(R,\epsilon)}{\pi}. \tag{15}$$

We have used the S-matrix computed at the lowest scattering energy, $\epsilon = 0.001$ H. We next compare the effective quantum numbers using quantum defects from scattering, $\nu_{n,\alpha}(R) = n - \mu^\alpha(R)$, with those extracted from bound-state calculations. The adiabatic potential-energy curves of the neutral $[V_i(R)]$ and ionic $[V_{\mathrm{ion}}(R)]$ molecules are computed at the same level as used in the electron-scattering calculations. The effective quantum numbers from the structure calculations are then given by

$$\nu_i(R) = \frac{1}{\sqrt{2[V_{\mathrm{ion}}(R) - V_i(R)]}}. \tag{16}$$

In Fig. 1, the effective quantum numbers from structure calculations are shown with gray curves for electronic states in $^2\Sigma^+$ symmetry. The red curves show the ones we obtained using quantum defects from scattering data for $n = 2$, 3, and 4. In the electron-scattering calculation, spherical harmonics corresponding to $l = 0$, 1, 2 are included, and hence, the $4f$ Rydberg state is not described. The effective quantum numbers from our structure calculation agree well with the results

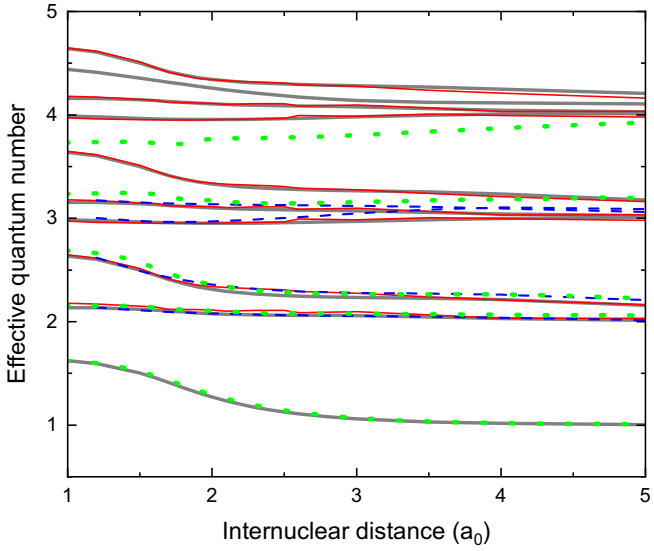

FIG. 1. Effective quantum numbers of NeH extracted from the present structure calculations in $^2\Sigma^+$ symmetry (gray curves). The blue dashed curves are the results from structure calculations by Petsalakis *et al.* [12] (blue dashed curves), while the green dotted curves are those by Hassaine *et al.* [13]. The red curves are the effective quantum numbers generated using adiabatic quantum defects from the electron-scattering calculations.

from the scattering. We also have very good agreement with quantum defects extracted from bound-state calculations by Petsalakis *et al.* [12] (blue dashed curves). We have reasonable agreement with the recent calculation by Hassaine *et al.* [13] (green dotted curves) for the $n = 2$ Rydberg states but not for the higher-lying Rydberg states.

The DR cross section of NeH^+ is calculated using the MQDT approach outlined above. In Fig. 2, the cross section when only the vibrational part of the frame transformation is included is displayed by the blue curve. In the absence of the direct mechanism, electron capture into the Rydberg states causes peaks in the cross section, similar to what has been found in, e.g., DR of HeH^+ [3,26,29] and H_3^+ [42]. The contributions to the NeH^+ DR cross sections from S-matrices in overall $^2\Pi$ and $^2\Delta$ symmetries are negligible in comparison to the $^2\Sigma^+$ symmetry. In the following calculations, the $^2\Pi$ and $^2\Delta$ symmetries are neglected.

The gray curve shows the DR cross section for the $NeH^+(v_0 = 0, j_0 = 0)$ ion including the full rovibrational frame transformation. The rotational motion causes additional structures in the cross section at low energies. As in other systems that lack a strong direct mechanism, it is important to include the rotational motion in the description to accurately describe the low-energy DR. Finally the red curve shows the DR cross section assuming a population of the rotational states given by a room temperature ($T = 300$ K) Boltzmann distribution.

To enable a comparison with the DR rate coefficient measured in the ASTRID storage ring [14], we compute the quantity $\alpha^{mb}(E) = \langle \tilde{\sigma} v \rangle$, where the DR cross section $\tilde{\sigma}$ is obtained assuming that the populations of the rotational states of NeH^+ follow a room-temperature Boltzmann distribution

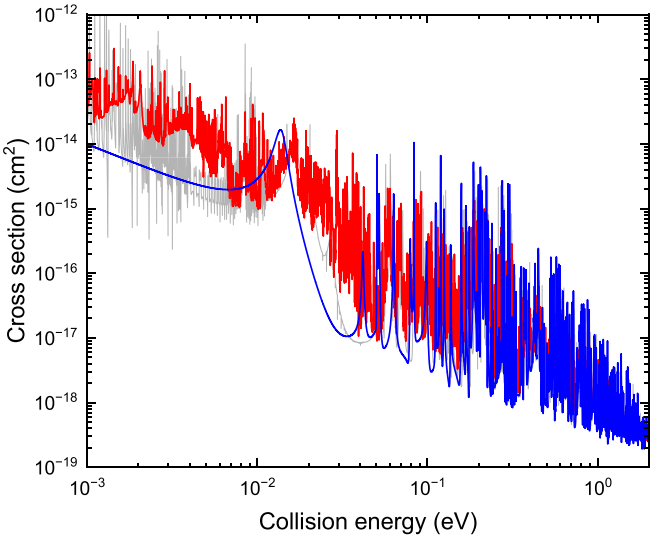

FIG. 2. Calculated DR cross sections for NeH^+. The gray curve shows the cross section for ions in the initial state $(v_0, j_0) = (0, 0)$. The red curve corresponds to the cross section averaged over the rotational states of the ion, assuming a Boltzmann population distribution at $T = 300\,\mathrm{K}$. The blue curve represents the DR cross section obtained without including the rotational part of the frame transformation.

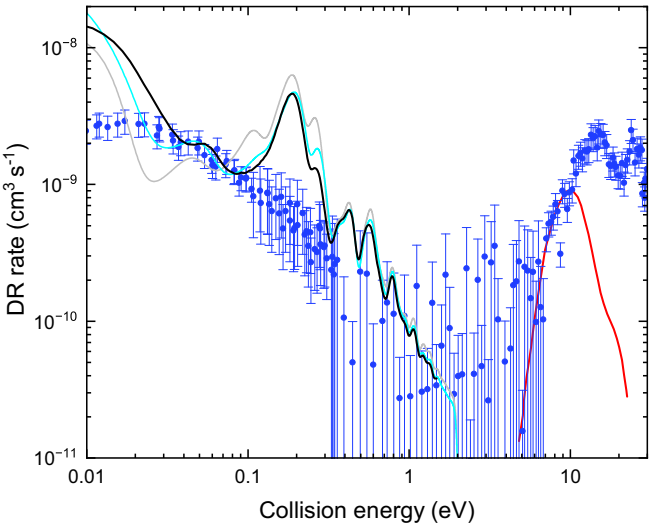

FIG. 3. The black curve shows the NeH^+ DR rate coefficient from the MQDT calculation assuming a Boltzmann distribution of the rotational-state populations. Gray and cyan curves display calculated rate coefficients for ions in rotational states $j = 0$ and $j = 1$, respectively. The red curve shows the rate coefficient for direct dissociation through electronic resonant states [7,14], and the blue circles represent the measured DR rate, normalized to the calculated value at 10 eV.

(red curve in Fig. 2). This assumption is rather crude: Calculated lifetimes of the low-lying rovibrational states of NeH^+ [14] indicate that the ions do not have sufficient time to reach thermal equilibrium before the experiment begins. A detailed analysis of the rovibrational-state populations has, however, not been carried out.

The DR rate is computed using longitudinal and transverse electron-beam temperatures of $kT_\parallel = 0.5\,\mathrm{meV}$ and $kT_\perp = 25\,\mathrm{meV}$, respectively, as reported in Ref. [14]. Figure 3 displays the calculated DR rate coefficients for NeH^+ in rotational states $j = 0$ and $j = 1$. There is a significant rotational effect on the DR rate coefficient. The rate coefficient obtained assuming a Boltzmann distribution of target rotational states is displayed by the thick black curve.

Figure 3 also includes (red line) the rate coefficient for direct dissociation via electronic resonant states. These direct DR cross sections were obtained in Refs. [7,14] using wave-packet propagation on complex potential-energy curves of the resonant electronic states. In the experiment, the absolute DR rate was not measured; only relative rates were obtained [7,14]. In Fig. 3, the measured rate is therefore scaled to match the previously calculated [14] DR rate coefficient for the direct process at a collision energy of $E = 10\,\mathrm{eV}$. As seen, there is an increase in the measured cross section above approximately 6 eV when the resonant states start to contribute.

Overall, the shape of the measured DR rate is not in satisfactory agreement with the calculated rate. At low energies, the measured rate shows a weaker energy dependence, and the pronounced structure near 0.2 eV predicted by the calculations is absent from the experimental data. A more reliable comparison between experiment and theory would require a realistic modeling of the rotational-state populations of NeH^+ in the ASTRID experiment—an analysis that lies beyond the scope of the present work.

As described in Sec. II, the DR cross section is here computed directly using the S-matrix extracted from fixed-nuclei electron-scattering calculations. The mixing between the partial waves (l, m) is then automatically included by the off-diagonal elements of $S^{\Lambda}_{l'm',lm}$. An alternative approach is to use quantum defects extracted from bound-state structure calculations in the MQDT computation. Then it is common to neglect the mixing of the partial waves. To test the validity of this approximation, the DR cross section for $NeH^+(v_0 = 0)$ is compared with the one obtained from the MQDT calculation assuming the fixed-nuclei scattering matrix elements are given by $\mathbf{S}(R) = \exp[2i\mu^\alpha(R)]$, where $\mu^\alpha(R)$ is the diagonal matrix containing the eigenvalues of the quantum defect matrix. In both calculations, the rotational part of the frame transformation is neglected, and the resulting cross sections are displayed in Fig. 4. For DR of NeH^+, the contribution from partial-wave mixing is significant at low energies. This can be understood by analyzing the quantum defect matrix $\mu(R)$ that has off-diagonal elements with significant R dependences.

In Fig. 5, the DR cross sections (including the rovibrational frame transformation) are displayed for the $(v_0, j_0) = (0, 0)$ states of the isotopologues $^{20}NeH^+$ and $^{20}NeD^+$.The DR cross section for NeD^+ is lower in magnitude, reflecting a smaller tunneling probability for the heavier isotopologue. Additionally, the resonances are shifted, reflecting the shifts of the rovibrational states of the target ion.

B. ArH^+

The scattering matrix obtained from fixed-nuclei electron-scattering calculations for ArH^+ is used to extract eigenquantum defects as described above. In Fig. 6, the effective quantum numbers using these eigenquantum defects

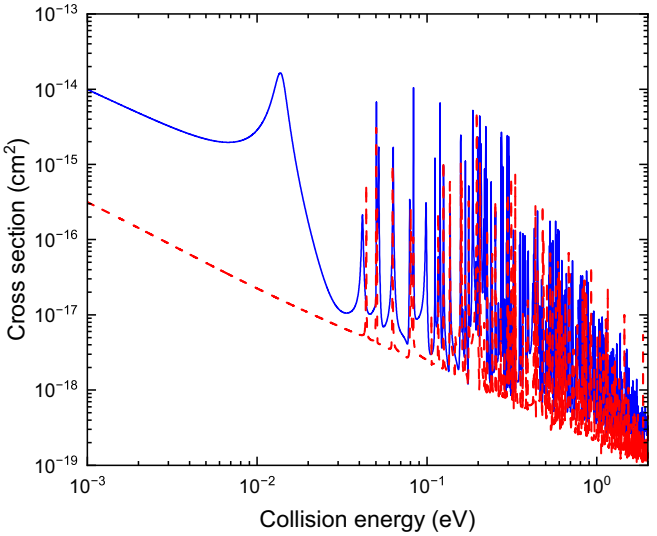

FIG. 4. Calculated DR cross sections for $NeH^+(v_0 = 0)$, including the vibrational part of the frame transformation (solid blue curve). The red dashed curve shows the DR cross section when partial-wave mixing is neglected and the *S*-matrix is constructed using eigenquantum defects.

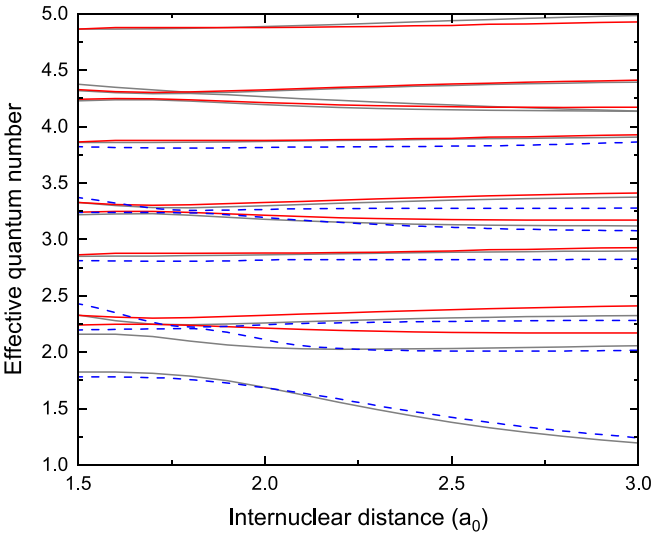

FIG. 6. Effective quantum numbers of the $^2\Sigma^+$ states of ArH. Gray curves correspond to the present structure calculations, blue dashed curves correspond to the results of Kirrander *et al.* [19], and red curves correspond to values obtained using eigenquantum defects from electron-scattering calculations.

(red curves) are compared with those obtained from bound-state calculations (gray curves) at the same level of theory for electronic states of $^2\Sigma^+$ symmetry. Like for NeH, the agreement is good.The results also satisfactorily agree with the quantum defects obtained from a bound-state calculation of the ArH Rydberg states by Kirrander *et al.* [19] (displayed by dashed blue curves).

The calculated DR cross section for ArH^+, including only the vibrational part of the frame transformation, is displayed by the blue curve in Fig. 7. Note that in comparison to NeH^+, the low-energy DR cross section of ArH^+ is 2 orders of magnitude smaller at a collision energy of 1 meV. In the ArH system, only the ground electronic state is open for dissociation at low energies. In NeH, electronic states dissociating into both Ne + H($n = 1$) and Ne + H($n = 2$) are energetically open at zero collision energy for the $NeH^+(v_0 = 0, j_0 = 0)$ target ion.

The black and red curves in Fig. 7 show the DR cross section obtained for the $ArH^+(v_0 = 0, j_0 = 0)$ and $ArH^+(v_0 = 0, j_0 = 1)$ ions including the full rovibrational frame transformation. Inclusion of the rotational motion of the target ion significantly increases the magnitude of the ArH^+ DR cross section at low energies (<0.01 eV).

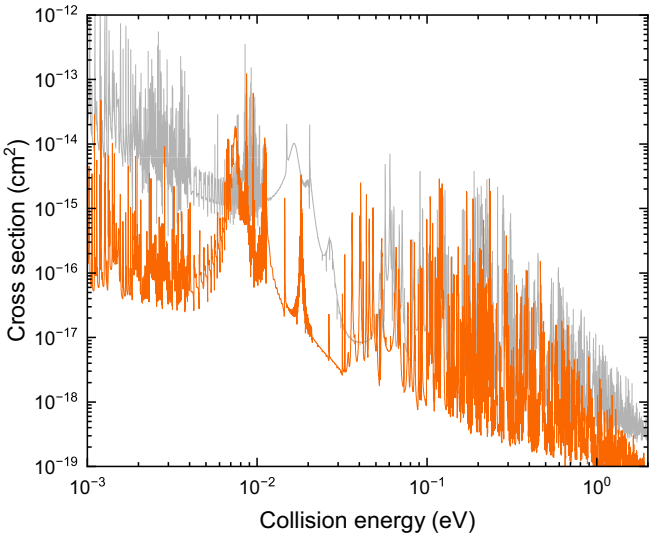

FIG. 5. Calculated DR cross sections for $NeH^+(v_0 = 0, j_0 = 0)$ (gray curve) and $NeD^+(v_0 = 0, j_0 = 0)$ (orange curve).

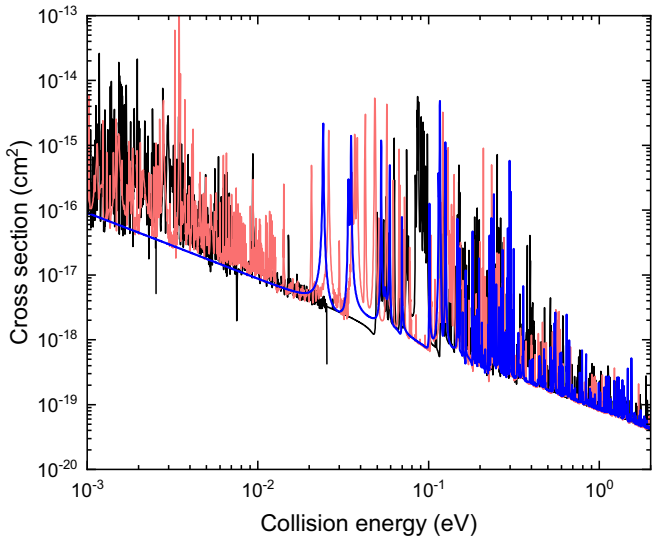

FIG. 7. Calculated cross sections for DR of ArH^+. The cross section for ions in $(v_0, j_0) = (0, 0)$ and is $(v_0, j_0) = (0, 1)$ are shown with the black and red curves, respectively. The blue curve is the DR cross section without inclusion of the rotational part of the frame transformation.

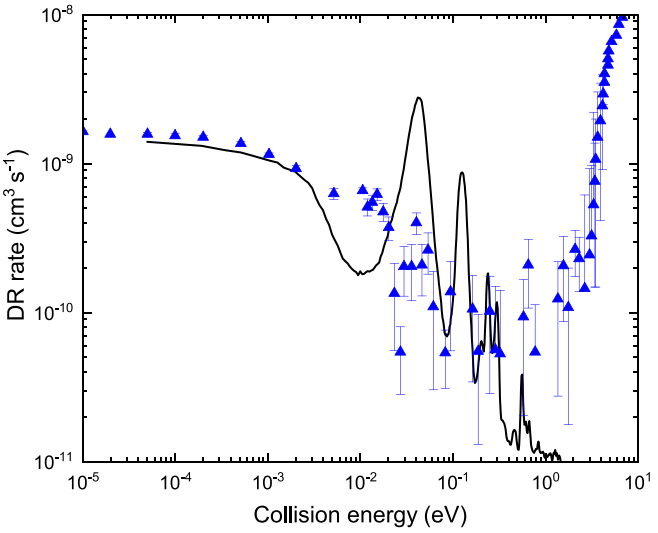

FIG. 8. Calculated (black line) and measured (blue triangles) DR rate coefficients for ArH^+. The calculated rate assumes populations of the lowest three rotational states of the ion.

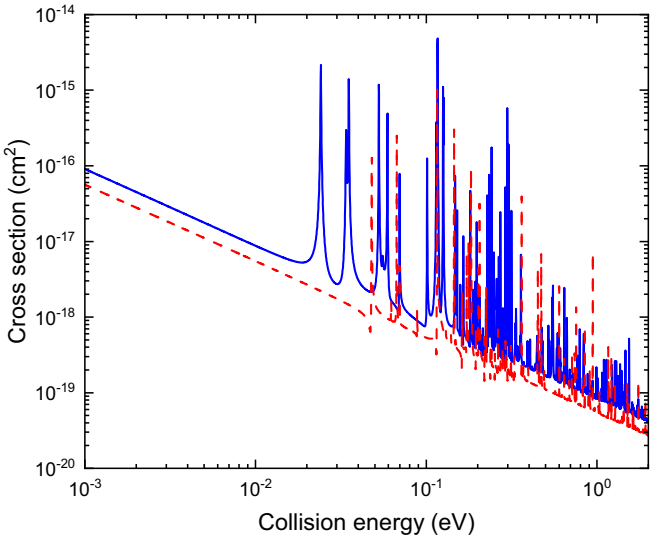

FIG. 9. DR cross section for ArH^+ calculated using the vibrational frame transformation. The blue curve shows the cross section with partial-wave mixing included, and the red dashed curve shows it when it is emitted and the eigenquantum defects are used.

To make a comparison with the measured DR rate coefficient from the CSR experiment [18], the DR rate [Eq. (14)] is calculated using the MQDT cross sections, assuming the three lowest rotational states ($j_0 = 0, 1, 3$) of ArH^+ have populations $p_0 = 0.57$, $p_1 = 0.37$, and $p_2 = 0.06$. It is estimated using a collisional-radiative model of the CSR experiment [18]. In Fig. 8, the calculated DR rate is displayed (black curve) and compared with the measured rate (blue triangles).At low collision energies ($E < 3$ meV), the magnitude of the calculated DR rate agrees very well with the measured rate. The computed rate has more pronounced structures than the measured one.

Above 2 eV, the measured DR rate increases significantly. This increase was also observed in the measurement using the ASTRID storage ring [14], and the rise of the cross section agrees with previous MQDT calculations by Hassaine *et al.* [13]. At these energies, DR for ArH^+ is driven by electron capture into electronic resonant states that become open for dissociation at 1.9 eV. This mechanism is not included in the present study. At energies > 3.9 eV, the CSR rate is the sum of the DR rate and the rate for dissociative excitation ($ArH^+ + e^- \rightarrow Ar + H^+ + e^-$) since they cannot be distinguished in the CSR experiment [18].

The influence of partial-wave mixing is investigated by computing the DR cross section using the eigenquantum defects. Only the vibrational part of the frame transformation is included, and in Fig. 9, the calculated rate using the full S-matrix (blue curve) is compared with the one obtained using eigenquantum defects (red dashed curve).By neglecting partial-wave mixing the DR cross section is slightly reduced.

Finally, we investigate the DR cross section for the various isotopologues of ArH^+. The experiments were performed on $^{40}ArH^+$ [14,18]. However, in interstellar space both $^{36}ArH^+$ and $^{38}ArH^+$ have been observed [43–45]. We perform the MQDT calculations on DR for $^{36}ArH^+$, $^{38}ArH^+$, $^{40}ArH^+$, and $^{40}ArD^+$ The calculations are performed for the ions in the $(v_0 = 0, j_0 = 0)$ rovibrational states, and the full rovibrational frame transformation is included. The DR cross sections for the $^{36}ArH^+$, $^{38}ArH^+$, and $^{40}ArH^+$ ions are very similar in magnitude and shape. In Fig. 10, the $^{40}ArH^+$ DR cross section (black curve) is compared with the one for $^{40}ArD^+$ (orange curve). Similar to NeH^+, the deuterium-containing isotopologue has, for most energies, a somewhat smaller cross section due to the larger reduced mass.

In a storage ring experiment, the rate α^{mb} is measured, and to help determine whether the differences in the DR cross sections for the different isotopologues are measurable, the DR rates for ArH^+ and ArD^+ (assuming $v_0 = 0$, $j_0 = 0$) are computed. The rates are shown in Fig. 11 with black and orange curves, respectively.Since the narrow resonant structures in the cross sections are averaged out when the DR rates are

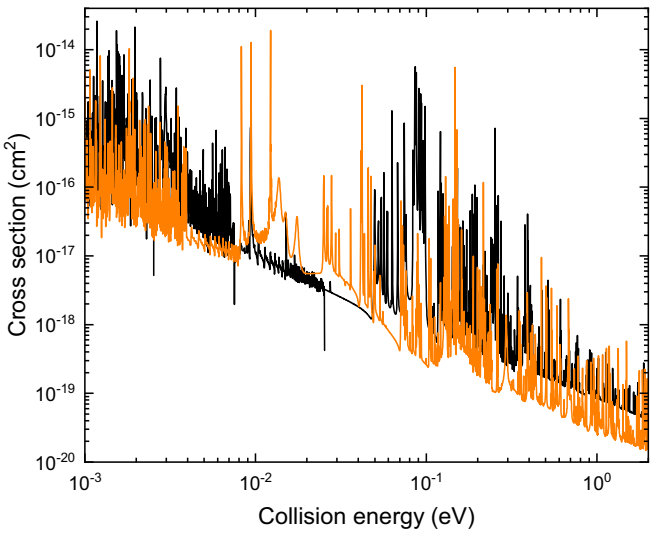

FIG. 10. Calculated DR cross sections for $^{40}ArH^+(v_0 = 0, j_0 = 0)$ (black curve) and $^{40}ArD^+(v_0 = 0, j_0 = 0)$ (orange curve).

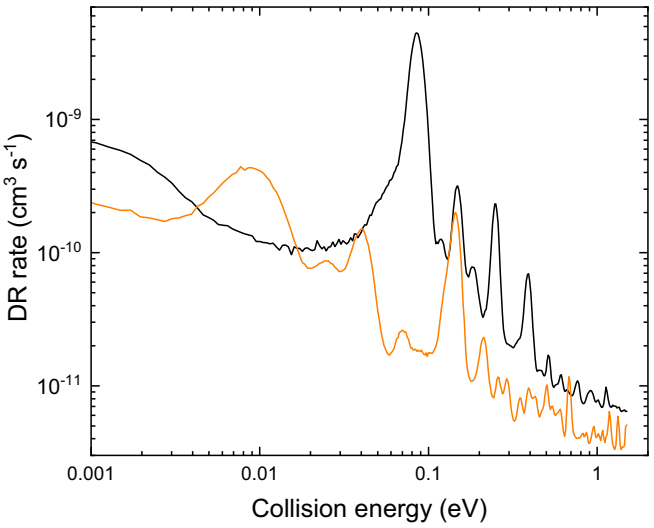

FIG. 11. Rate coefficient for DR of $ArH^+(v_0 = 0, j_0 = 0)$ (black curve) and $ArD^+(v_0 = 0, j_0 = 0)$ (orange curve).

calculated, there are measurable differences between the rates for the two isotopologues. For a detailed comparison with measured rates, it is, however, crucial to accurately account for the populations of the ions' rotational states in the experiment.

V. CONCLUSIONS

Like in the HeH system, low-energy ($E < 2$ eV) dissociative recombination of ArH^+ and NeH^+ proceeds primarily through electron capture into bound Rydberg states. The process was investigated here using multichannel quantum defect theory, with dissociation via Rydberg states treated using exterior complex scaling when calculating the vibrational states of the target ions. Fixed-nuclei scattering matrices were obtained from electron-ion-scattering calculations performed with the complex Kohn variational method, with the coordinate origin placed at the center of charge of the target ions.

The results demonstrate that both rotational motion and partial-wave mixing play important roles in the DR dynamics. Similar effects have been demonstrated in, e.g., DR of HeH^+ [3] and CH^+ [20]. For ArH^+, the calculated DR rate shows satisfactory agreement with experimental measurements from the CSR ion storage ring [18].

To achieve a complete theoretical description of ArH^+ and NeH^+ DR that describes the processes at both low and intermediate collision energies, a unified treatment of the resonant and nonresonant processes—similar to that in [20]—should be undertaken. Furthermore, the energy dependence of the quantum defects should be carefully addressed [46].

ACKNOWLEDGMENTS

The work by Å.L. was initiated during her sabbatical at the Max Planck Institute for Nuclear Physics (MPIK) in Heidelberg, Germany. We acknowledge O. Novotný and H. Kreckel for directing us to this interesting problem and for supplying us with experimental rate coefficients and generating DR rates from calculated cross sections to compare with measurements. Å.L. acknowledges support from both MPIK and Stockholm University for making the sabbatical possible. Additionally, valuable discussions with C. H. Greene and V. Kokoouline are acknowledged.

DATA AVAILABILITY

The data that support the findings of this article are openly available [47].

[1] O. Novotný, *et al.*, Quantum-state–selective electron recombination studies suggest enhanced abundance of primordial HeH^+, Science **365**, 676 (2019).
[2] S. L. Guberman, Dissociative recombination without a curve crossing, Phys. Rev. A **49**, R4277 (1994).
[3] R. Čurík, D. Hvizdoš, and C. H. Greene, Dissociative recombination of cold HeH^+ ions, Phys. Rev. Lett. **124**, 043401 (2020).
[4] C. Strömholm, J. Semaniak, S. Rosén, H. Danared, S. Datz, W. van der Zande, and M. Larsson, Dissociative recombination and dissociative excitation of $^4HeH^+$: Absolute cross sections and mechanisms, Phys. Rev. A **54**, 3086 (1996).
[5] T. Tanabe, I. Katayama, S. Ono, K. Chida, T. Watanabe, Y. Arakaki, Y. Haruyama, M. Saito, T. Odagiri, K. Hosono, K. Noda, T. Honma, and H. Takagi, Dissociative recombination of isotopes with an ultra-cold electron beam from a superconducting electron cooler in a storage ring, J. Phys. B **31**, L297 (1998).
[6] J. B. A. Mitchell, O. Novotny, G. Angelova, J. L. LeGarrec, C. Rebrion-Rowe, A. Svendsen, L. H. Andersen, A. I. Florescu-Mitchell, and A. E. Orel, Dissociative recombination of rare gas hydride ions: I. NeH^+, J. Phys. B **38**, 693 (2005).
[7] V. Ngassam, A. I. Florescu-Mitchell, and A. E. Orel, Electron-induced resonant dissociation and excitation of NeH^+ and NeD^+, Phys. Rev. A **77**, 042706 (2008).
[8] L. Carata, A. E. Orel, and A. Suzor-Weiner, Dissociative recombination of He_2^+ molecular ions, Phys. Rev. A **59**, 2804 (1999).
[9] J. Royal and A. E. Orel, Dissociative recombination of He_2^+, Phys. Rev. A **72**, 022719 (2005).
[10] V. Ngassam and A. E. Orel, Dissociative recombination of Ne_2^+ molecular ions, Phys. Rev. A **73**, 032720 (2006).
[11] G. Theodorakopoulos, R. J. Buenker, and I. D. Petsalakis, Theoretical investigation of the excited states of NeH: Calculations of dipole transition moments and radial coupling matrix elements, J. Phys. B **20**, 5335 (1987).
[12] I. D. Petsalakis, G. Theodorakopoulos, Y. Li, G. Hirsch, R. J. Buenker, and M. S. Child, Theoretical study on the Rydberg states of NeH: *Ab initio* quantum defect and complex coordinate calculations, J. Chem. Phys. **108**, 7607 (1998).
[13] R. Hassaine, D. Talbi, R. P. Brady, J. Z. Mezei, J. Tennyson, and I. F. Schneider, Theoretical study of the excited states of NeH and of their non-adiabatic couplings: A preliminary for the modeling of the dissociative recombination of NeH^+, J. Chem. Phys. **162**, 134302 (2025).
[14] J. B. A. Mitchell, O. Novotny, J. L. LeGarrec, A. Florescu-Mitchell, C. Rebrion-Rowe, A. V. Stolyarov, M. S. Child, A. Svendsen, M. A. E. Ghazaly, and L. H. Andersen, Dissociative recombination of rare gas hydride ions: II. ArH^+, J. Phys. B **38**, L175 (2005).

[15] A. Abdoulanziz, F. Colboc, D. A. Little, Y. Moulane, J. Z. Mezei, E. Roueff, J. Tennyson, I. F. Schneider, and V. Laporta, Theoretical study of ArH^+ dissociative recombination and electron-impact vibrational excitation, Mon. Not. R. Astron. Soc. **479**, 2415 (2018).

[16] E. Djuissi, A. Bultel, J. Tennyson, I. F. Schneider, and V. Laporta, Electron collisions with ArH^+ molecular ions: Highly excited vibrational states and dissociative excitation, Plasma Sources Sci. Technol. **31**, 114012 (2022).

[17] R. von Hahn, *et al.*, The cryogenic storage ring CSR, Rev. Sci. Instrum. **87**, 063115 (2016).

[18] A. Kálosi, M. Grieser, L. W. Isberner, H. Kreckel, Å. Larson, D. A. Neufeld, A. E. Orel, D. Paul, D. W. Savin, S. Schippers, V. C. Schmidt, A. Wolf, M. G. Wolfire, and O. Novotný, Dissociative recombination of rotationally cold ArH^+, Phys. Rev. A **110**, 022816 (2024).

[19] A. Kirrander, M. S. Child, and A. V. Stolyarov, *Ab initio* and quantum-defect calculations for the Rydberg states of ArH, Phys. Chem. Chem. Phys. **8**, 247 (2006).

[20] J. Forer, D. Hvizdoš, X. Jiang, M. Ayouz, C. H. Greene, and V. Kokoouline, Unified treatment of resonant and nonresonant mechanisms in dissociative recombination: Benchmark study of CH^+, Phys. Rev. A **107**, 042801 (2023).

[21] P. Saxe, B. H. Lengsfield III, R. Martin, and M. Page, MESA (Molecular Electronic Structure Applications) (1990).

[22] T. N. Rescigno, B. H. Lengsfield, III, and C. W. McCurdy, *The Incorporation of Modern Electronic Structure Methods in Electron-Molecule Collision Problems: Variational Calculations Using the Complex Kohn Method* (World Scientific, Singapore, 1995), pp. 501–588.

[23] T. N. Rescigno, C. W. McCurdy, A. E. Orel, and B. H. Lengsfield, III, *The Complex Kohn Variational Method* (Plenum, New York, 1995), pp. 1–44.

[24] H. T. Dunning and P. T. Hay, in *Gaussian Basis Sets for Molecular Calculations*, edited by H. F. Schaefer (Plenum, New York, 1977), pp. 1–28.

[25] P. Siegbahn and B. Liu, An accurate three-dimensional potential energy surface for H_3, J. Chem. Phys. **68**, 2457 (1978).

[26] H. Takagi and M. Tashiro, Study on the dissociative recombination of HeH^+ by multi-channel quantum defect theory, EPJ Web Conf. **84**, 02002 (2015).

[27] R. Čurík and C. H. Greene, Inelastic low-energy collisions of electrons with HeH^+: Rovibrational excitation and dissociative recombination, J. Chem. Phys. **147**, 054307 (2017).

[28] A. D. McLean and G. S. Chandler, Contracted Gaussian basis sets for molecular calculations. I. second row atoms, Z = 11–18, J. Chem. Phys. **72**, 5639 (1980).

[29] R. Čurík and C. H. Greene, Indirect dissociative recombination of LiH^+ molecules fueled by complex resonance manifolds, Phys. Rev. Lett. **98**, 173201 (2007).

[30] E. S. Chang and U. Fano, Theory of electron-molecule collisions by frame transformations, Phys. Rev. A **6**, 173 (1972).

[31] A. Scrinzi and N. Elander, A finite element implementation of exterior complex scaling for the accurate determination of resonance energies, J. Chem. Phys. **98**, 3866 (1993).

[32] C. W. McCurdy, M. Baertschy, and T. N. Rescigno, Solving the three-body Coulomb breakup problem using exterior complex scaling, J. Phys. B **37**, R137 (2004).

[33] T. N. Rescigno and C. W. McCurdy, Numerical grid methods for quantum-mechanical scattering problems, Phys. Rev. A **62**, 032706 (2000).

[34] D. C. Brody, Biorthogonal quantum mechanics, J. Phys. A **47**, 035305 (2014).

[35] A. Vibok and G. G. Balint-Kurti, Parametrization of complex absorbing potentials for time-dependent quantum dynamics, J. Phys. Chem. **96**, 8712 (1992).

[36] N. Y. Du and C. H. Greene, Quantum defect analysis of HD photoionization, J. Chem. Phys. **85**, 5430 (1986).

[37] F. Matsushima, Y. Ohtaki, O. Torige, and K. Takagi, Rotational spectra of $^{20}NeH^+$, $^{20}NeD^+$, $^{22}NeH^+$, and $^{22}NeD^+$, J. Chem. Phys. **109**, 2242 (1998).

[38] J. W. Brault and S. P. Davis, Fundamental vibration-rotation bands and molecular constants for the ArH^+ ground state ($^1\Sigma^+$), Phys. Scr. **25**, 268 (1982).

[39] H. Odashima, A. Kozato, F. Matsushima, S. Tsunekawa, and K. Takagi, Far-infrared rotational spectrum of ArD^+, J. Mol. Spectrosc. **195**, 356 (1999).

[40] M. Cueto, J. Cernicharo, M. J. Barlow, B. M. Swinyard, V. J. Herrero, I. Tanarro, and J. L. Doménech, New accurate measurement of $^{36}ArH^+$ and $^{38}ArH^+$ ro-vibrational transitions by high resolution IR absorption spectroscopy, Astrophys. J. Lett. **783**, L5 (2014).

[41] A. Kálosi, L. Gamer, M. Grieser, R. von Hahn, L. W. Isberner, J. I. Jäger, H. Kreckel, D. A. Neufeld, D. Paul, D. W. Savin, S. Schippers, V. C. Schmidt, A. Wolf, M. G. Wolfire, and O. Novotný, Dissociative recombination of rotationally cold OH^+ and its implications for the cosmic ray ionization rate in diffuse clouds, Astrophys. J. Lett. **955**, L26 (2023).

[42] V. Kokoouline and C. H. Greene, Unified theoretical treatment of dissociative recombination of D_{3h} triatomic ions: Application to H_3^+ and D_3^+, Phys. Rev. A **68**, 012703 (2003).

[43] M. J. Barlow, B. M. Swinyard, P. J. Owen, J. Cernicharo, H. L. Gomez, R. J. Ivison, O. Krause, T. L. Lim, M. Matsuura, S. Miller, G. Olofsson, and E. T. Polehampton, Detection of a noble gas molecular ion, $^{36}ArH^+$, in the Crab nebula, Science **342**, 1343 (2013).

[44] P. Schilke, D. A. Neufeld, H. S. P. Müller, C. Comito, E. A. Bergin, D. C. Lis, M. Gerin, J. H. Black, M. Wolfire, N. Indriolo, J. C. Pearson, K. M. Menten, B. Winkel, A. Sánchez-Monge, T. Möller, B. Godard, and E. Falgarone, Ubiquitous argonium (ArH^+) in the diffuse interstellar medium: A molecular tracer of almost purely atomic gas, Astron. Astrophys. **566**, A29 (2014).

[45] A. M. Jacob, K. M. Menten, F. Wyrowski, B. Winkel, and D. A. Neufeld, Extending the view of ArH^+ chemistry in diffuse clouds, Astron. Astrophys. **643**, A91 (2020).

[46] D. Hvizdoš, C. H. Greene, and R. Čurík, Backpropagated frame transformation theory: A reformulation, Phys. Rev. A **101**, 012709 (2020).

[47] Å. Larson, Cross sections for dissociative recombination of ArH^+ and NeH^+ calculated using MQDT, Stockholm University [Dataset] (2025), https://doi.org/10.17045/sthlmuni.30675314.v1.